Article

Structure and Surface Morphology Effect on the Cytotoxicity of [Al$_2$O$_3$/ZnO]$_n$/316L SS Nanolaminates Growth by Atomic Layer Deposition (ALD)

D. Osorio [1], J. Lopez [2], H. Tiznado [3], Mario H. Farias [3], M. A. Hernandez-Landaverde [4], M. Ramirez-Cardona [5], J. M. Yañez-Limon [4], J. O. Gutierrez [6], J. C. Caicedo [7] and G. Zambrano [1,*]

[1] Thin Films Group, Universidad del Valle, Cali C.P. 76001, Colombia; marcelamateriales@gmail.com
[2] CONACYT—Centro de Nanociencias y Nanotecnología, Universidad Nacional Autónoma de México, Ensenada, B.C, Av. Insurgentes Sur 1582, Ciudad de Mexico C.P. 03940, Mexico; javierlo21@cnyn.unam.mx
[3] Centro de Nanociencias y Nanotecnología (CNyN), Universidad Nacional Autónoma de México (UNAM), Km 107 Carretera Tijuana-Ensenada s/n. B. C., Mexico C.P. 22800, Mexico; tiznado@cnyn.unam.mx (H.T.); mario@cnyn.unam.mx (M.H.F.)
[4] Centro de Investigación y de Estudios Avanzados del I.P.N., Unidad Querétaro, Libramiento Norponiente No. 2000, Fracc. Real de Juriquilla, Querétaro Qro. C.P. 76230, Mexico; martinhernandez@cinvestav.mx (M.A.H.-L.); jmyanez@cinvestav.mx (J.M.Y.-L.)
[5] Área Académica de Ciencias de la Tierra y Materiales, Universidad Autónoma del Estado de Hidalgo (UAEH), Ciudad del Conocimiento, Col. Carboneras, Mineral de la Reforma Hgo. C.P. 42184, Mexico; mariusr@uaeh.edu.mx
[6] Farmacología Univalle, Universidad del Valle, Cali C.P. 76001, Colombia; jose.gutierrez@correounivalle.edu.co
[7] TPMR Group, Universidad del Valle, Cali C C.P. 76001, Colombia; julio.cesar.caicedo@correounivalle.edu.co
*   Correspondence: gustavo.zambrano@correounivalle.edu.co

check for updates

Abstract: Recently, different biomedical applications of aluminum oxide (Al$_2$O$_3$) and zinc oxide (ZnO) have been studied, and they have displayed good biocompatible behavior. For this reason, this study explores nanolaminates of [Al$_2$O$_3$/ZnO]$_n$ obtained by atomic layer deposition (ALD) on silicon (100) and 316L stainless steel substrates with different bilayer periods: n = 1, 2, 5, and 10. The intention is to correlate the structure, chemical bonds, morphology, and electrochemical properties of ZnO and Al$_2$O$_3$ single layers and [Al$_2$O$_3$/ZnO]$_n$ nanolaminates with their cytotoxic and biocompatibility behavior, to establish their viability for biomedical applications in implants based on the 316L SS substrate. These nanolaminates have been characterized by grazing incident X-ray diffraction (XRD), finding diffraction planes for wurtzite type structure from zincite. The chemical bonding and composition for both single layers were identified through X-ray photoelectron spectroscopy (XPS). The morphology and roughness were tested with atomic force microscopy (AFM), which showed a reduction in roughness and grain size with a bilayer period increase. The thickness of the samples was measured with scanning electron microscopy, and the results confirmed the value of ~210 nm for the nanolaminate samples. The electrochemical impedance spectroscopy analysis with Hank's balanced salt solution (HBSS) evidenced an evolution of [Al$_2$O$_3$/ZnO]$_n$/316L system corrosion resistance of around 95% in relation with the uncoated steel substrate as function of the increase in the bilayers number. To identify the biocompatibility behavior of these nanolaminate systems, the lactate dehydrogenase test was performed with Chinese hamster ovary (CHO) cells for a short system of life cell evaluation. This test shows the cytotoxicity of the multilayer compared to the single layers of Al$_2$O$_3$, ZnO, and 316L stainless steel. The lowest cytotoxicity was found in the single layers of ZnO, which leads to cell proliferation easier than Al$_2$O$_3$, obtaining better adhesion and anchoring to its surface.
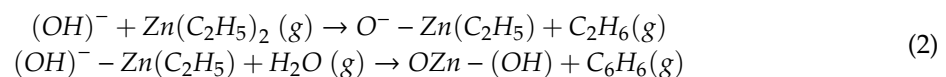
1. Introduction

Multilayer systems show the best interaction with different materials of natural origin for a specific use. An example of this is the nanolaminates of different thin film oxides. These forms have many utilities and have been studied for their magnetic, electrical, optical, mechanical, electrochemical, and biocompatible properties. However, to explore the potential applications of nanolaminates it is relevant that nanostructures have novel properties compared to thicker films or bulk material, especially given that the conjugation of the number of interfaces and the nature of the multilayer system happens in the same way as the superlattice systems [1]. The consistency of the atomic layer deposition (ALD) films lies in the gas phase thin film deposition method, as a modification of chemical vapor deposition (CVD). For the ALD process, the precursor material is led into the chamber by alternating cycles or pulses, where any cycles are separated by an inert gas purging or by evacuation in high-vacuum reactors [1]. The precursors react on the substrate surface according to the process conditions, and when some precursors are self-limited it leads to a controlled film growth by surface saturated reactions. An example of these is the nanolaminates of aluminum oxide (Al$_2$O$_3$)/zinc oxide (ZnO) deposited by ALD [2–8], which has improved the optical or mechanical behavior of the single layer with the bilayers number increase [9–11]. Both materials come from self-limiting organometallic precursors such as trimethyl-aluminum (TMA) and diethylzinc (DEZ), and both represent a scheme for other applications using the individual potential of single Al$_2$O$_3$ and ZnO layers. For the electro-catalytic process, both oxides have been studied with glucose oxidation [12]; even the mechanical properties of these oxides are important to notice because their multilayer structure leads to an increase in hardness and toughness with the bilayer period according to the Hall-Petch effect [9]. Biocompatible behavior is an important property for these materials too; ZnO has been studied to check its biocompatibility and biosafety, and in some cases, it is considered to be a nanosensor for implantable biomedical detections [13]. Some authors have shown their cell viability for many potential applications [8,14–18]. Similarly, Al$_2$O$_3$ exhibits a biocompatible behavior and is a standard ceramic–ceramic articulation material, due to its hardness and its least wear compared to metals, it has been used as the femoral head for joint replacement through decades [13,19].

Given that both ZnO and Al$_2$O$_3$ show biocompatible behavior, it would be interesting to show how these materials can be approached and what kind of interactions can be obtained for the nanolaminates of both materials. Especially, to improve the mechanical behavior, wear rate or biocompatible behavior in multilayer system, as it is the objective of this study. This study used the atomic layer deposition (ALD) technique. Through this process, aluminum oxide (Al$_2$O$_3$) and zinc oxide (ZnO) was deposited in the form of nanostructured layers with the same ratio between the single layers and different bilayer periods (λ), for the same final thickness of the Al$_2$O$_3$/ZnO bilayers. The ALD technique has emerged as a process to obtain thin films in the nanoscale regimen [20,21] with the advance in semiconductors, especially for oxides in metal oxide semiconductor field effect Transistor (MOSFET) structures, capacitors for dynamic random access memory (DRAM), integrated circuits and other microelectronic devices [20,22]. Many studies on ALD report that it can obtain novel materials grown with good thickness uniformity and conformality into three-dimensional structures, however, some of its potential applications could be for protective coatings, as anti-corrosive films for biocompatible films [23,24] In this work, we want to study the effect on the structure, chemical bonds, morphology, and electrochemical properties of ZnO and Al$_2$O$_3$ single layers and [Al$_2$O$_3$/ZnO]$_n$ multilayer nanolaminates system deposited on 316L SS substrate. The above will correlate with its cytotoxic and biocompatibility behavior to establish its viability for biomedical applications in implants based on the 316L SS substrate.

2. Experimental Details

Multilayers or Al_2O_3/ZnO nanolaminates were deposited by the atomic layer deposition technique, with a Beneq (Espoo, Uusimaa, Finland) TFS 200 ALD reactor using gas precursors of thrymetilaluminum (TMA, Strem 93-1360) and diethylzinc (DEZ, Aldrich 256781), so that during each cycle, thicknesses of 1.2 Å and 2 Å can be obtained for the Al_2O_3 and ZnO layers, respectively. Ultra high purity (UHP) nitrogen (99.999%) was introduced to the chamber as a carrier/purge gas with 1×10^{-12} ppm and a flow rate of 250 sccm. For all of the processes a constant substrate temperature of 200 °C and a ~1.5 mbar reactor pressure were used. Vapor deionized water was the oxidant agent.

Si (100) and 316L stainless steel used as substrates were previously adapted and cleaned to prevent any contamination on the surface. To achieve this, mechanical polishing and chemical cleaning were used. First, the 316L stainless steel (316L SS) was mechanically machined to obtain flat discs of 1 mm thickness and 1 cm of diameter. Later, these steel substrates, together with those of silicon, were cleaned in acetone with ultrasound for 15 min at 50°C, then rinsed with an isopropanol reagent grade, and finally dried with UHP N_2. To obtain the Al_2O_3 layer, cycles of 150 ms TMA dose, 750 ms N_2 purge, and 150 ms DI water dose were introduced into the chamber, and then 500 ms N_2 purge for the vacuum process. The chemical reactions with the TMA follow the Equation (1) [25,26]. Afterward, UHP N_2 purge the chamber before starting another cycle. Similarly, to obtain ZnO layers, 30 ms DEZ dose, 2 s N_2 purge, 150 ms DI water dose, and 500 ms N_2 purge, are needed. These react through Equation (2) [27–29] to obtain an atomic layer per cycle.

$$2Al(CH_3)_3 + 3H_2O \rightarrow Al_2O_3 + 3CH_4 \tag{1}$$

$$(OH)^- + Zn(C_2H_5)_2\,(g) \rightarrow O^- - Zn(C_2H_5) + C_2H_6(g)$$
$$(OH)^- - Zn(C_2H_5) + H_2O\,(g) \rightarrow OZn - (OH) + C_6H_6(g) \tag{2}$$

The processes described were repeated in many cycles, as the thickness needs to complete the film. These $[Al_2O_3/ZnO]_n$ nanolaminates were deposited with a thickness ratio of 1:1, for a total thickness set constant with a nominal value of ~200 nm and different bilayers period n (1, 2, 5, and 10). The above means that the thickness of each ZnO and Al_3O_3 layer was 100, 50, 20, or 10 nm for n = 1, 2, 5, and 10 bilayer periods, respectively. Figure 1 shows a scheme of the $[Al_2O_3/ZnO]_n$ multilayer structure obtained during the ALD process.
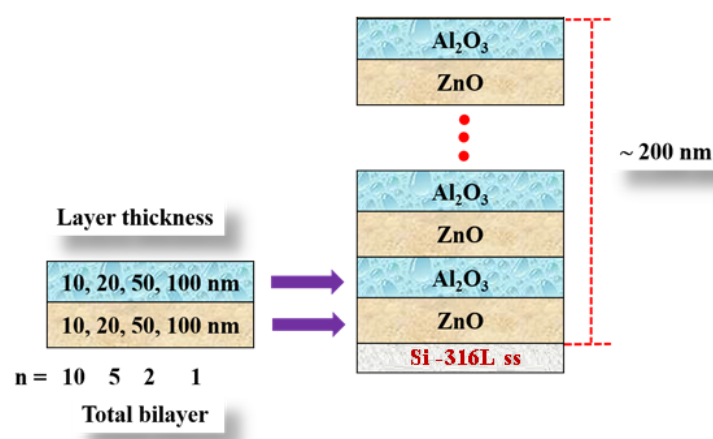

Figure 1. Experimental configurations for the [aluminum oxide (Al_2O_3)/zinc oxide (ZnO)]$_n$ multilayer structure.

Different methods were used to characterize the nanolaminate systems of Al_2O_3 and ZnO single layers, deposited onto silicon and 316 SS substrates. Phase identification of ALD deposited layers on silicon substrate (100) was accomplished by patterns obtained from grazing incidence X-ray diffraction (GIXRD) experiments (Ultima IV diffractometer, RIGAKU, Akishima-shi, Tokyo, Japan).

The experiments were conducted on a RIGAKU Ultima IV diffractometer, using CuK$\alpha_{1,2}$ radiation (1.5406 Å/1.5444 Å doublet wavelength generated by an X-ray tube operating at 40 kV and 30 mA), in a 2θ range from 22° to 72°, a step scan of 0.02° and an integration time of 0.5 s per step. The parallel incident beam was fixed at an angle of 1° with the sample surface. To determine the chemical composition, X-ray photoelectron spectroscopy was employed using a JEOL JPS 9200 spectrometer (Tokyo, Japan) with monochromatic Al Kα line. The roughness and surface morphology were studied using atomic force microscopy (AFM) (XE 70, Santa Clara, CA, USA). The SEM instrument was a JEOL JIB-4500 (Hesperia, CA, USA) Focused Ion Beam Scanning Electron Microscope and the Field Emission Electron TEM microscope (JEOL, Peabody, MA, USA) was a JEOL JEM-2100F. For TEM analysis, the witness sample growth on Si(100) substrate was examined.

Additionally, the electrochemical behavior of $[Al_2O_3/ZnO]_n$/316L SS system was studied by the electrochemical impedance spectroscopy (EIS) method in the presence of a Hank's balanced salt solution (HBSS). Finally, the cytotoxicity test lactate dehydrogenase (LDH) used gave us a first summary of the biocompatibility for these materials. The electrochemical study was carried out with a Gamry unit, model PCI 4, utilized for DC and AC measurements. Electrochemical impedance spectroscopy (EIS) and Tafel polarization curves were obtained at room temperature, using a cell with a working electrode within an exposed area of 1 cm^2, a reference electrode (Ag/AgCl), and a platinum wire counter-electrode under Hank´s balanced salt solution (HBSS) for an exposure time of 30 min. For Nyquist diagrams, the frequency sweep was performed in the range from 100 kHz to 0.001 Hz using sinusoidal voltage amplitude of 10 mV applied to the working electrode (sample) and reference electrode. To obtain Tafel polarization curve diagrams a voltage sweep was carried out at a speed of 0.5 mV/s in the range of −0.25 to 0.25 V. To determine the roughness and grain size of the top layer, an MFP-3D Asylum Research atomic force microscope (AFM) was used.

A cytotoxicity test provides information about direct cell interaction with a chemical compound, pharmaceutics, or biomaterials. There are many methods in the literature related to cytotoxicity tests. A cytotoxicity test was carried out with a lactate dehydrogenase (LDH) kit plus version 0.6, Roche, Mannhelm, Germany [30], which provides a simple, reliable colorimetric method for quantifying cellular cytotoxicity by the liberation of lactate dehydrogenase (plasma membrane damage releases LDH into the cell culture media [31] Chinese hamster ovary (CHO) cell cultures were done to obtain 50,000 cells/well, for use in triplicate samples. For the cytotoxicity test, a 24-well plate with different distributions for the sample was available, as well as for the positive (releasable triton) and negative controls in this LDH assay. These cell cultures were deposited on the surface of ZnO, Al_2O_3, $[Al_2O_3/ZnO]_n$/316L SS substrate, and copper was used as a positive cytotoxic control. After 24 h the cytotoxic LDH was applied to the culture, and the reaction mixture gets incubated for 30 min until a stop solution was applied. The enzymatic assay was performed in the supernatant and it was measured in an Elisa spectrometer, with an absorbance reading from 450 to 630 nm. The absorbance readings for each the samples were compared to a control reagent for positive and negative cytotoxicity, for this LDH kit the Equation (3) was used [30].

$$Cytotoxicity\ (\%) = \frac{Exp.Value - low\ control}{high\ control - low\ control} \times 100 \tag{3}$$

Finally, for the cell adhesion analysis to the surface of the samples after spending 48 h in contact with them, a cell fixation process was used employing histological techniques using a mixture of 3% glutaraldehyde (GA) in phosphate-buffered solution (PBS) to maintain the osmolarity and pH of the aqueous solution of the cells. After this process, the surface of the samples was analyzed under the scanning electron microscope.

3. Results

3.1. X-ray Diffraction Analysis

For comparative purposes, a GIXRD study of nanolaminates growth on Si (100) wafer, and 316L SS substrate is carried out. Figure 2 shows the diffraction patterns of Al_2O_3 and ZnO single layers, and $[Al_2O_3/ZnO]_n$ nanolaminates with n = 1, 2, 5 and 10, for both 316L SS (Figure 2a) and Si(100) (Figure 2b) wafer substrates. The corresponding GIXRD single-layer patterns corroborated the expected amorphous nature of Al_2O_3. ZnO, for both a single layer or in multilayers, crystallizes on wurtzite-type structure (zincite, space group $P6_3mc$, $a = b$ = 3.24982 Å, c = 5.20661 Å, $\alpha = \beta = 90°$, $\gamma = 120°$, from JCPDS card 36-1451 [32]). In the case of the steel-substrate, its patterns clearly exemplified the main peaks of α- and γ-Fe forms. For samples growth onto the Si wafer, its (100) peak was slightly detected, and the specific combination between the incident grazing angle (1°) and the sample orientation in the holder produced the low intensity of that peak. Patterns from the ZnO single layer deposited directly on the substrate showed multiaxial preferred orientation models: (100)/(002) and (100)/(002)/(103) for 316L SS and Si substrates, respectively; and only the principal preferred orientation—i.e., PO on (002) plane of zincite—was maintained through the $[Al_2O_3/ZnO]_n$ nanolaminate samples. The former two PO's models are the result of the different substrates' interaction.
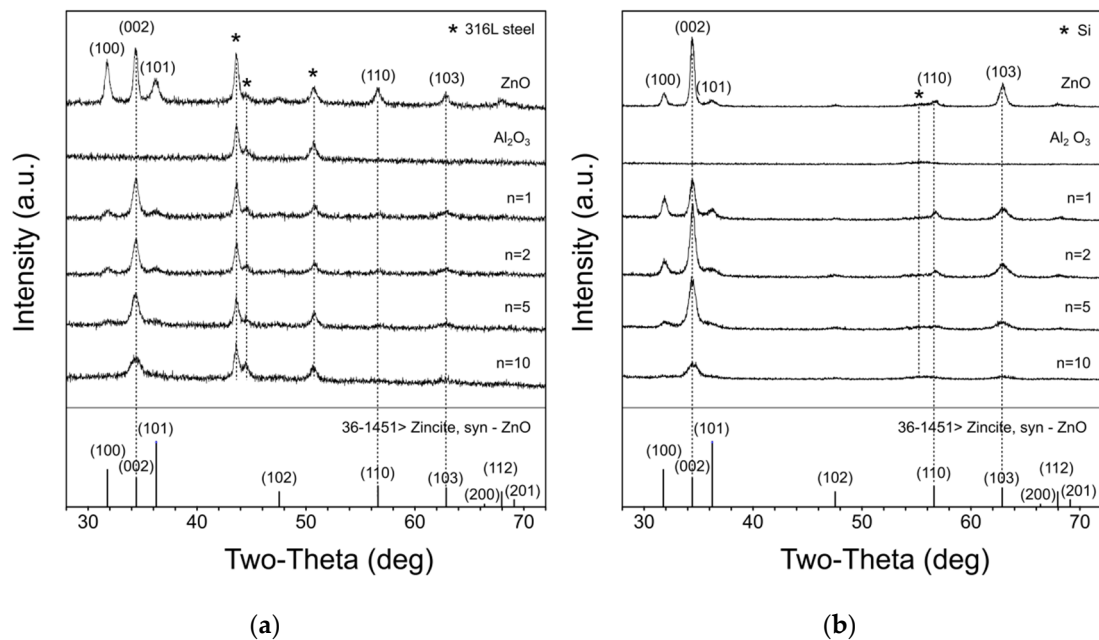

Figure 2. Grazing incidence X-ray diffraction (GIXRD) patterns for ZnO and Al_2O_3 single layers, and $[Al_2O_3/ZnO]_n$ multilayer (*n* = 1, 2, 5, and 10) samples deposited on (**a**) 316L SS and (**b**) silicon (100) substrates.

Refinement of the unit-cell, full width at half maximum (FWHM), and shape parameters were achieved by the LeBail-based "pattern matching" method implemented in the *Fullprof* program. Likewise, the determination of the crystallite size was carried out by combining FWHM peak-analysis—the instrumental resolution was derived from calibration on powdered Si provided by National Institute of Standards and Technology (NIST)—using the Debye-Scherrer equation, and software Jade MDI 9.7 (Table 1).

Table 1. Zincite lattice parameters and crystallite size in both single and multilayers growths on Si(100) wafer and 316L SS.

Substrate	Sample	Lattice Parameters (Å)		Crystallite Size$_{(002)}$ (Å)
		$a = b$	c	
Si(100)	ZnO	3.2450(4)	5.2044(3)	383(4)
	$(Al_2O_3/ZnO)_1$	3.2416(8)	5.2028(7)	197(4)
	$(Al_2O_3/ZnO)_2$	3.2397(8)	5.2018(1)	267(6)
	$(Al_2O_3/ZnO)_5$	3.2467(13)	5.2042(7)	179(4)
	$(Al_2O_3/ZnO)_{10}$	3.2569(19)	5.1988(11)	93(3)
316L SS	ZnO	3.2530(23)	5.2163(24)	428(9)
	$(Al_2O_3/ZnO)_1$	3.265(122)	5.2166(31)	226(4)
	$(Al_2O_3/ZnO)_2$	3.2492(35)	5.2156(12)	221(8)
	$(Al_2O_3/ZnO)_5$	3.2558(55)	5.2208(15)	175(6)
	$(Al_2O_3/ZnO)_{10}$	3.2662(165)	5.2186(32)	79(3)

() Estimated Standard Deviation—ESD.

The trend to a crystallite-size diminution as n increases was proved from $n = 2$ to $n = 10$, for both substrates, Si and 316L SS. This behavior is explained in terms of the diffusivity of Al/Al_2O_3 into the overlaid crystalline zincite. The extent of atomic diffusion increased with a higher number of interlayer interphases or thinner layers. The subsequent influence on defects-related phenomena (e.g., microstrains or crystalline lattice distortions) with concomitant disruption of crystal growth was evidenced by the broadening of GIXRD peaks [33]. On the other hand, this increase of crystal-growth disruptions phenomena was not observed when $n = 2$ nanolaminate samples are compared with the $n = 1$ counterpart. The crystallite size in $n = 2$ showed a higher value in the case of samples with a silicon substrate, 267 Å (i.e., a percentage increase of 36%). It practically remained unchanged for the steel-substrate sample, 221 Å. The first-deposited Al_2O_3 layer appears here as a diffusion barrier when $n = 2$; its relatively high thickness (i.e., ~ 52 nm) compromised diffusivity effects and, consequently, precluded the occurrence of crystalline defects. The experimental design to growth nanolaminates plays a crucial role in this discussion since the total thickness of the different-n nanolaminates remains constant (i.e., ~210 nm). The proper thickness of Al_2O_3 or ZnO layers varied in each growing experiment. Taking into consideration that the experiments were conducted on selected values of n (1, 2, 5, and 10), the 52 nm-thickness of the first-deposited Al_2O_3 layer in the $[Al_2O_3/ZnO]_2$ nanolaminate could mark a behavior threshold from which (in terms of n, for $n \geq 2$), the crystallite size of wurtzite-type ZnO decreases. The crystallite sizes when $n = 1$—i.e., 197 and 226 Å for growths on silicon single-crystal wafer and 316L stainless steel, respectively—were notably inferior to those without overlying Al_2O_3. Although this behavior indicates ZnO growth rates higher in nanolaminates than in single layers growth on the primary substrates, former cases were mainly governed by the diffusion effects mentioned above.

Regardless the particular crystallite-size of zincite in $[Al_2O_3/ZnO]_n$ nanolaminates, it is worth underlining that the outstanding highest values (see Table 1) correspond to the ZnO layer deposited directly on the primary substrates, 383 and 428 Å for Si and 316L SS, respectively. These values are comparable with those from ZnO film growth by different techniques reported elsewhere: spray pyrolysis, ultrasonic spray, and pulsed laser deposition [34–36].

3.2. X-ray Photoelectron Spectroscopy Analysis

The chemical composition and binding energy of the elements were determined with X-ray photoelectron spectroscopy (XPS). Figure 3a,b show the XPS survey scans from Al_2O_3 and ZnO samples,

respectively, displaying the signals of the elements on their surfaces. The more intense signals are due to the O, Al, and Zn elements; even so, traces of carbon are present.
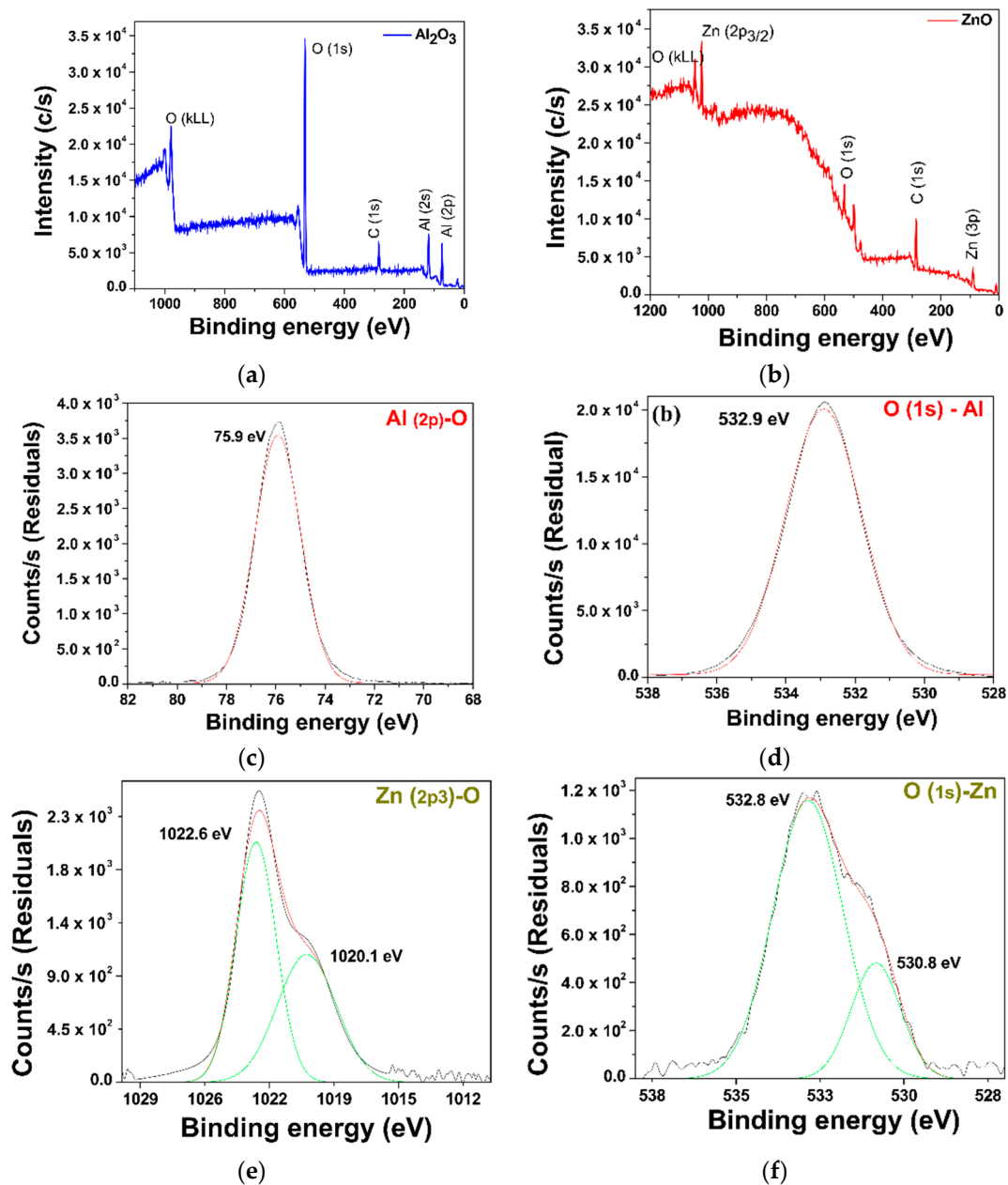

Figure 3. XPS survey spectra and high-resolution signals for single layers: (**a**) survey spectra AlxO1−x, (**b**) survey spectra Zn-O, (**c**) Al 2p, (**d**) O 1s (Al$_2$O), (**e**) Zn (2p3) signals and (**f**) O 1s signal (ZnO).

Figure 3c shows the high-resolution XPS spectra of the Al$_2$O$_3$ single layer, evidencing the oxygen signal (O 1s). Similarly, Figure 3d shows the high-resolution spectra corresponding to aluminum in the Al 2p region. The Al 2p signal related to Al$_2$O$_3$ has been observed with a binding energy of 74.5 eV [37]. This particular binding energy position corresponds to the Al$_2$O$_3$ phase formation [38]. The high-resolution signal of the O 1s was found at a binding energy of 533 eV [39].

Figure 3c–f shows the experimental data as scatter plots and solid lines which are the best fit for two Gaussian functions; the deconvoluted plots are also shown in these graphs. Figure 3e,f correspond to the high-resolution spectra associate with the ZnO layer. The first signal was assigned to the O 1s and the second signal corresponds to Zn 2p$_{3/2}$ element. The ZnO was adjusted with two peaks,

the first one is located around 1020.7 eV and the second one is located around 1022.6 eV attributed to Zn $2p_{3/2}$ [32,40]. Considering the last discussion, it was possible to determine that the stoichiometric relations for alumina- and zinc oxide-obtained layers correspond approximately to $Al_{0.4}O_{0.6}$ and $Zn_{0.4}O_{0.6}$, respectively. The fact that the surface of ZnO contains oxygen in a concentration higher than one-to-one with Zn could be due to environmental contamination during transporting from preparation to XPS measurement.

3.3. Atomic Force Microscopy (AFM)

Figure 4 exhibits the AFM surface topography associated with single layers and multilayers deposited on the 316L SS substrate, which shows the cluster formations. It can be observed that the morphological shapes on the samples surface and height surface decreases with the increase of bilayer numbers. This means a gradual decrease in roughness values. Moreover, the clusters and roughness in Figure 4c for the $[Al_2O_3/ZnO]_2$ nanolaminates present a combination of the growth of Al_2O_3 on ZnO layers [10,41].
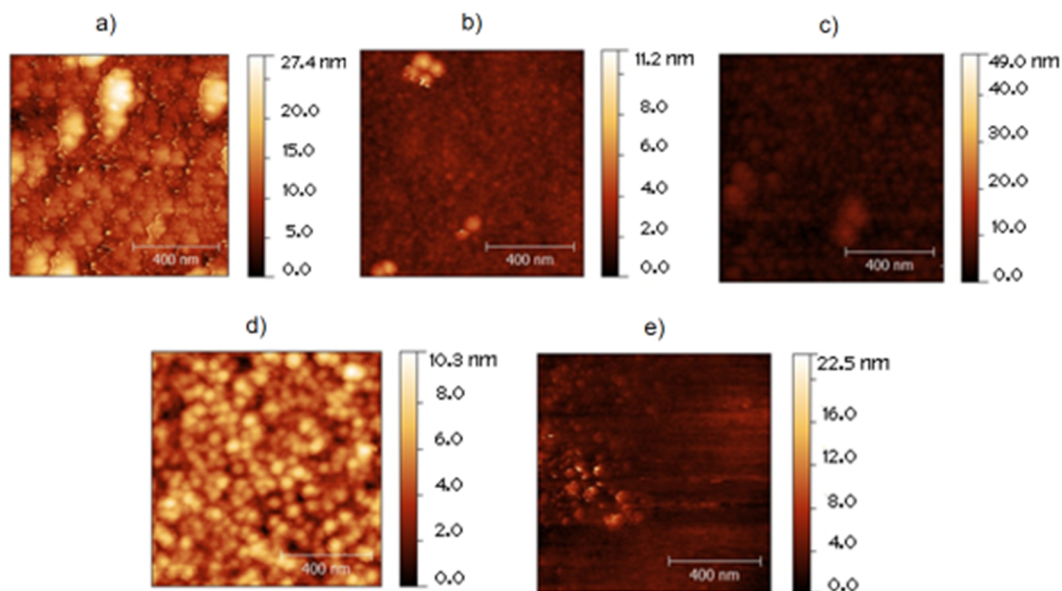

Figure 4. Surface topography for (**a**) ZnO, (**b**) Al_2O_3 single layers and (**c**) $[Al_2O_3/ZnO]_1$, (**d**) $[Al_2O_3/ZnO]_2$, and (**e**) $[Al_2O_3/ZnO]_5$ multilayers.

Figure 5 shows the reduction of the average roughness with the increase in the bilayer numbers. According to the restriction model, this is a behavior presented by the multilayers of a superlattice, because the increase in the number of bilayers with a constant total thickness represents a decrease in the bilayer period, and an increase in the number of the interfaces due to the decrease of the thickness of the bilayer. Figure 5 also shows that the grain size decreases with the increase of the number of bilayers. The grain size for the ZnO single layer was 89.3 nm, but we could not obtain this value for multilayers from the AFM measurements because the AFM measurements were carried out on the surface of the multilayers, where the upper layer was always the amorphous layer of Al_2O_3.
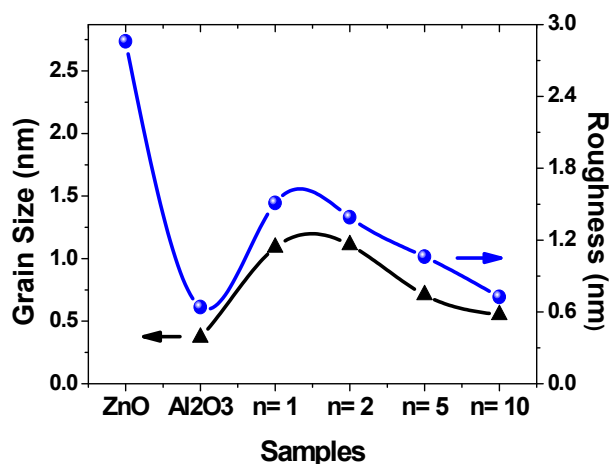
Figure 5. Roughness and grain size evolution of ZnO and Al_2O_3 single layers, and $[Al_2O_3/ZnO]_n$ bilayers with the increase of bilayers number.

3.4. TEM Analysis

Transmission electron microscopy (TEM) micrographs in the cross-sectional mode were obtained to validate and verify the total multilayer thickness. Figure 6a presents the TEM cross-sectional view of $[Al_2O_3/ZnO]_{10}$ multilayers, and Figure 6b shows a higher resolution image of two Al_2O_3/ZnO bilayers, where it was possible to corroborate the multilayers arrangement formation with 11.1 and 12.0 nm thickness for each ZnO and Al_2O_3 monolayers, respectively, and an average total thickness of approximately 210.0 nm. A change in the shade of the gray color could be observed, which is associated with a change in the electronic density of the materials in the multilayer stack. Therefore, the modulation of the grayscale change is associated with different layers, where the darker gray color is related to the ZnO layer. From image 6b, ZnO layer shows (002) interplanar distances around 0.260 nm, which is very close to that in the JCPDS card 36-1451, as well as in [32,41,42]. The amorphous growth of the Al_2O_3 layer is evident in the same figure.}
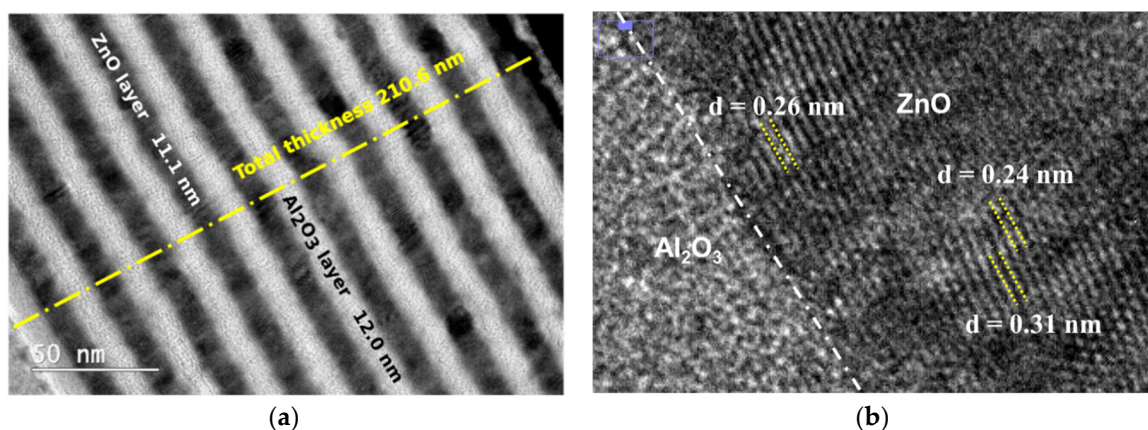

(**a**)

(**b**)

Figure 6. TEM cross-sectional views of $[Al_2O_3/ZnO]_n$ bilayers (**a**) *n* = 10 and (**b**) higher resolution image of an Al_2O_3/ZnO bilayer.

3.5. Electrochemical Analysis

The electrochemical behavior of the $[Al_2O_3/ZnO]_n/316L$ system was determined by the electrochemical impedance spectroscopy technique in the presence of Hank´s balanced salt solution (HBSS). Figure 7a displays the Nyquist diagram, the imaginary part of the impedance versus its real part, for the 316L stainless steel, ZnO, and Al_2O_3 single layers and $[Al_2O_3/ZnO]_n/316L$ multilayers. Figure 7b shows the equivalent circuit [43] simulating the substrate-coating and coating-electrolyte

interfaces, as a double layer capacitance in parallel with the coating resistance and the electrolyte resistance due to the ion transfer reaction from the electrolyte to the metallic substrate [44].
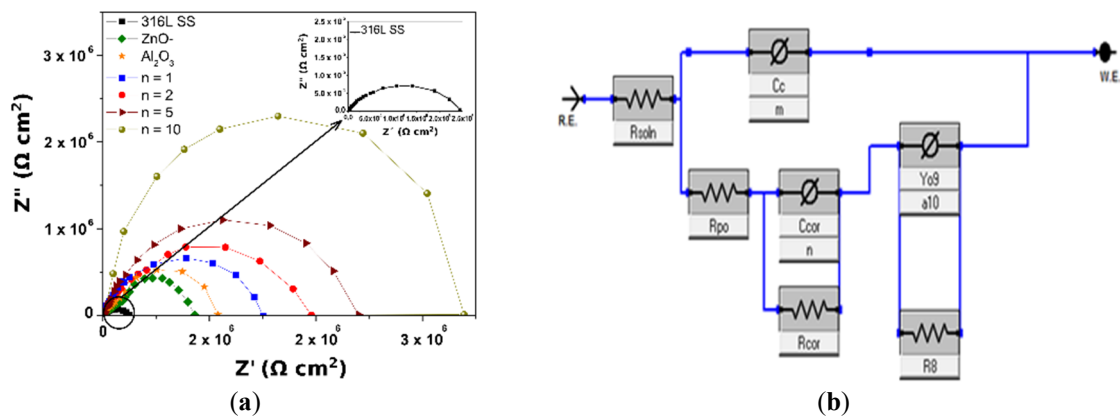

Figure 7. (**a**) Impedance diagrams of 316L stainless steel, ZnO and Al_2O_3 single layers and $[Al_2O_3/ZnO]_n/316L$ multilayers. The inset shows the Nyquist diagram of 316L SS. (**b**) Equivalent circuits used for simulation of the experimental data, where RE, RS, RP, CPE and WE are the reference electrode, electrolyte resistance, polarization resistance of coatings, the constant elements of phase, and the working electrode (the sample), respectively.

From the Nyquist diagrams and the equivalent circuit (Figure 7b), the values for the polarization resistance (R_p) were extracted. The results present in Figure 8b indicate that the polarization resistance increased with the increase of the bilayer number, confirming the protective effect of layers and multilayers.
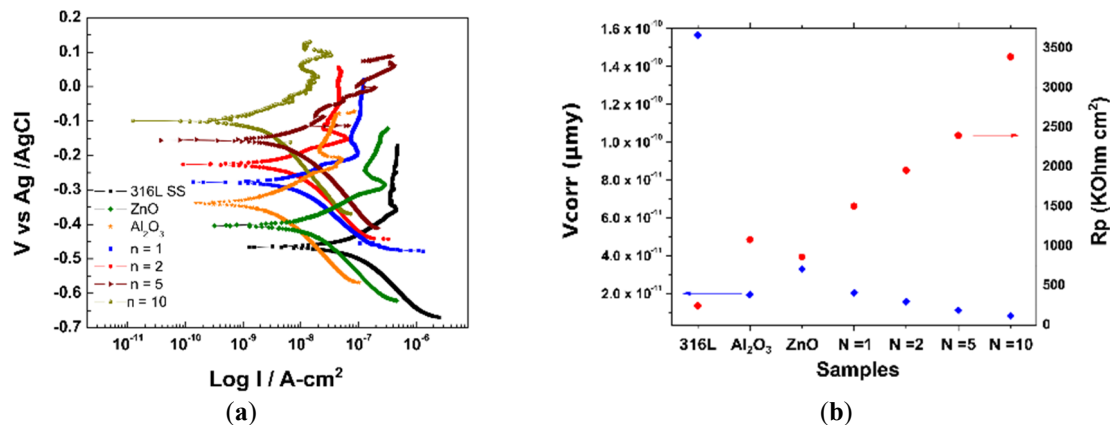

Figure 8. (**a**) Tafel polarization curves. (**b**) Polarization resistance (R_p) and corrosion rate, of 316L stainless steel, ZnO, and Al_2O_3 single layers and $[Al_2O_3/ZnO]_n/316L$ multilayers.

Figure 8a shows the Tafel polarization curves, where the corrosion potential is displayed as a function of the logarithm of the corrosion current density for the 316L stainless steel, ZnO, and Al_2O_3 single layers and $[Al_2O_3/ZnO]_n/316L$ multilayers. The curves for ZnO and Al_2O_3 single layers and $[Al_2O_3/ZnO]_n/316L$ multilayers were in the negative region of the corrosion potential. The above indicates that in any case there was ion transfer from the electrolyte to the metallic substrate, but it was less negative than for the 316L substrate, and it decreased with the increase in the $[Al_2O_3/ZnO]_n$ bilayer number. The slopes of the anodic and cathodic zones and the plateau region of the Tafel curves gave information about the corrosion rate. The plateau value increased strongly for the single layers and multilayers in comparison to that value from the uncoated 316L substrate, indicating that the coatings provided greater corrosion protection compared to uncoated 316L SS surface. Tafel polarization

curves were used to calculate the corrosion current density i_{corr} using the Stern-Geary model, with the Equation (4) [45].

$$i_{corr} = \frac{\beta_a \beta_c}{2.03 R_p (\beta_a + \beta_c)} \tag{4}$$

where β_a and β_c are the Tafel, anodic and cathodic slopes respectively, and R_p is the polarization resistance value obtained from the Nyquist diagram. However, the corrosion current can be directly related to the corrosion rate through the following Equation (5):

$$V_{corrosion} = 0.13 \, (i_{corr}) \left(\frac{W_e}{\rho} \right) \tag{5}$$

where: ρ is the density of the material in g/cm^3, W_e is the electrochemical equivalent of the molecular weight of the metal divided by the number of electrons involved in the anodic reaction. Finally, 0.13 is a constant that includes the Faraday constant and the conversion factor necessary to give the corrosion rate in micrometer per year ($\mu m/y$) when i_{corr} is expressed in $\mu A/m^2$.

The results presented in Figure 8b indicate that the polarization resistance increased and the corrosion rate diminished when the 316L SS substrate was covered with ZnO and Al_2O_3 single layers and with the increase of the $[Al_2O_3/ZnO]_n$ bilayer number, confirming the protective effect of the layers and multilayers against corrosion. The reason for this protective effect is related to the fact that the ZnO crystallites become smaller as the number of multilayers increases, and therefore the total number of grain boundaries in the ZnO material grows larger, giving a higher polarization resistance.

3.6. Lactate Dehydrogenase Test Analysis

The calculated values for cytotoxicity determined according to Equation (3) are shown in Figure 9b for the ZnO and Al_2O_3 single layers, $[Al_2O_3/ZnO]_n$ multilayer system, and the 316L SS. According to ISO 10993-531 [46,47] the results may show a low level of cytotoxicity or grade "2", which means a slight reactivity for the qualitative morphological qualification of the cytotoxicity of the sample, when the percentage of cytotoxicity does not exceed 60%; and a degree "1" or light reactivity when it has a value lower than 20%. The grade "0" will be for materials or extracts without reactivity. Based on this, we observed at 24 h that 316 SS was almost at the limit of mild reactivity with 51.3%; therefore, for short time applications, it could give a good response, but for longer terms, lower cytotoxicity is desirable. Al_2O_3 single layer exhibited similar behavior as 316L SS, with 40.3% of cytotoxicity given that the Al_2O_3 single layer is amorphous. A very different behavior was observed for ZnO single layer, which is crystalline and has the largest crystallite size (428 ± 9 Å). In this case, the cytotoxicity percentage was 1.6%, which is almost not reactive; this could mean either that ZnO has the lowest lysis effect in CHO cells for 24 h or that it does not interfere with the cell culture growth.

In the case of the multilayers, with $n = 1$ and $n = 2$, they presented a lower cytotoxicity behavior with a slight reactivity (grade "1"), a cytotoxicity percentage of 29.8% and 30.3%, respectively. This means that occasional lysed cells are present during assay, so few cell populations were damaged. While for $n = 5$ and $n = 10$, a mild reactivity was assumed, and they showed a cytotoxicity percentage of 38.5% and 38.0%, respectively.

The cytotoxicity dependence behavior of the samples with the number of bilayers is related to several factors, such as the ZnO/Al_2O_3 bilayers thickness, the crystallite size of the ZnO layer, and the roughness and amorphicity of the Al_2O_3 upper layer. Figure 9b shows the correlation between these factors. We can conclude that for $[Al_2O_3/ZnO]_n/316L$ multilayer structure, the samples with $n = 1$ and $n = 2$, ZnO's higher layer thicknesses (100 and 50 nm) and crystallite sizes (226 and 221 Å, respectively) show the lowest cytotoxicity compared to multilayers with a greater bilayer number ($n = 5$ and 10), where the ZnO thicknesses and crystallite size are smaller (175 and 79 Å, respectively). The above confirms the important role that the ZnO layer plays.
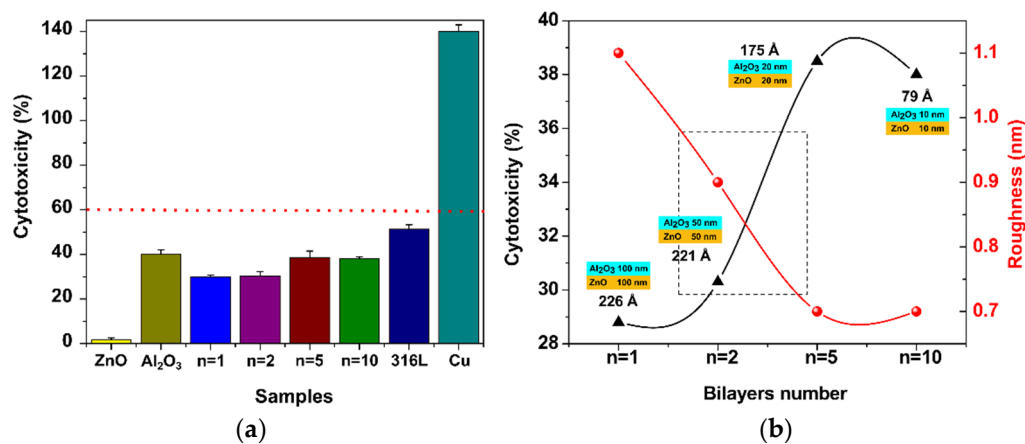
Figure 9. (**a**) Citotoxicity percentage for 316L stainless steel, ZnO, and Al$_2$O$_3$single layers and [Al$_2$O$_3$/ZnO]$_n$/316L multilayers. (**b**) [Al$_2$O$_3$/ZnO]$_n$/316L cytotoxicity behavior as a function of roughness of top Al$_2$O$_3$ layer, and crystallite size and thickness of the ZnO layer.

Summarizing, the LDH test for all samples showed low cytotoxicity levels under 60%, approved for short terms applications.

Figure 10 presents the cell adhesion SEM images for 316L/ZnO and 316L/Al$_2$O$_3$ monolayers and 316L/[Al$_2$O$_3$ /ZnO]$_n$ multilayers (n = 1, 2, 5, and 10). In these images it can be seen that the cell adhesion behavior to the surface was closely linked to the level of cytotoxicity of the samples (see Figure 9a). On the other hand, except for the 316L/[Al$_2$O$_3$ /ZnO]$_{10}$ multilayers, it can be observed that on the surface of the multilayers, groups of cells were closely linked between and to the surface, extending the fine anchor joints towards it, which allowed their correct fixing. This may be due to the Al$_2$O$_3$ top layer surface roughness (less than 1 nm) for all samples in the multilayer, which meant less anchoring for cells that needed it.
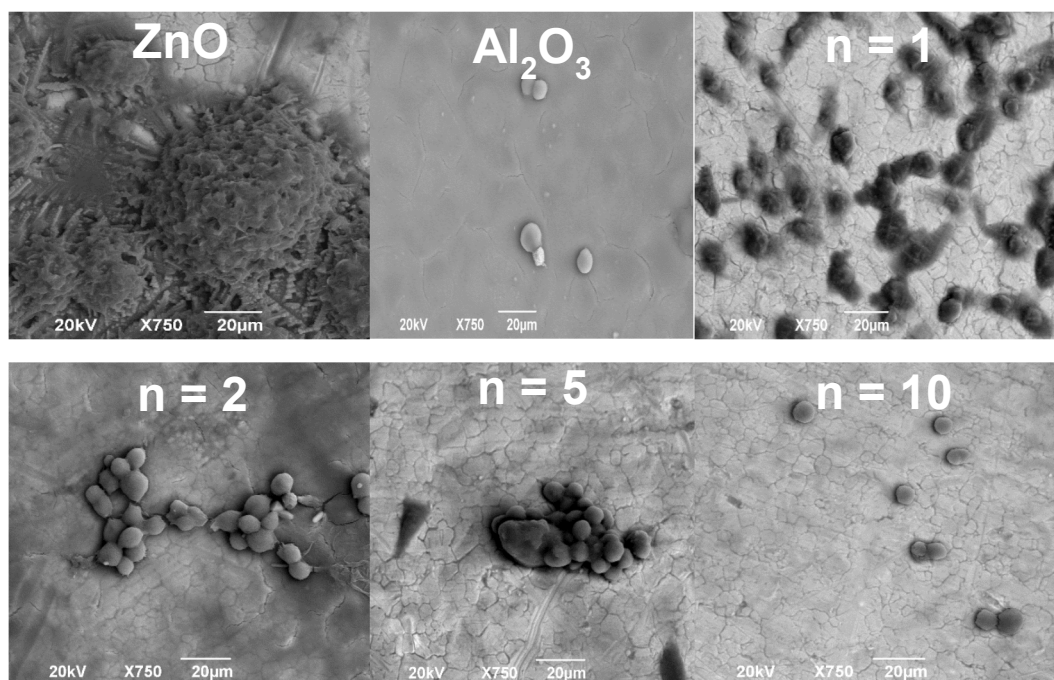

Figure 10. Cell adhesion scattering electron microscopy (SEM) images for ZnO and Al$_2$O$_3$ single layers and 316L/[Al$_2$O$_3$ /ZnO]$_n$ multilayers (n = 1, 2, 5, and 10).

Thus, if the CHO cells cannot adhere to a surface, they tend to disperse, floating on the fluid. Within a given time, cells need other cells to interact with them and survive as a group: if this does not happen, cell junctions break and they die. This does not mean samples were toxic, but that these surfaces are not adherent and could be used in applications such as acetabular prosthesis or for femoral head, where friction will be necessary to obtain normal activity for the patient.

For the sample of ZnO we did obtain a different behavior, since the CHO cells got anchored to the surface, which lead to a good cell interaction and union between them. This behavior develops a net of well-knitted cells, which will grow to confluence. The ZnO layer probably leads to a better adherent surface because its roughness is higher than Al_2O_3 roughness and gives more anchored points for the fixation of the cells. These kinds of surfaces could be used in other applications, for example, for femoral prosthesis replacement.

4. Conclusions

The structure, chemical bonds, morphology, and electrochemical properties of ZnO and Al_2O_3 single layers and the $[Al_2O_3/ZnO]_n$ nanolaminates system deposited on 316L SS, along with additional growths on Si(100) wafer for comparison, were studied to elucidate critical factors that determine their cytotoxicity and subsequent biocompatibility.

An amorphous alumina layer was always deposited overlaying on the zincite crystalline-type ZnO-layer of the $[Al_2O_3/ZnO]_n$ stack motifs of the nanolaminates. ZnO formed in $[Al_2O_3/ZnO]_n$ multilayers showed a decrease in its crystallite size due to the influence of the alumina that induces crystalline defects evidenced by a broadening of ZnO GIXRD-peaks (i.e., changes in FWHM), as well as a persistent preferred orientation on (002). Otherwise, the ZnO single layers exhibited the largest crystallite size. Concerning this behavior of crystallite size, no significant differences were appreciated between samples deposited on 316L SS or Si(100) substrates. AFM morphological analysis demonstrated that the grain size and roughness on the surface decreased as the $[Al_2O_3/ZnO]_n$ bilayer number increased (for $n > 2$), directly correlated with the concomitant decrease of crystallite size in ZnO.

Finally, the electrochemical study showed that corrosion resistance of $[Al_2O_3/ZnO]_n$ nanolaminates was higher in comparison with the 316L SS surface, and ZnO, and Al_2O_3 single layer, confirming the protective effect of the layers and multilayers against corrosion. This protective effect is because the ZnO crystallites become smaller as the number of multilayers increases, and therefore the total number of grain boundaries in the ZnO material grows larger, resulting in a higher polarization resistance.

According to LDH in CHO cells, the biocompatible behavior showed low cytotoxic responses. This means that the ZnO single layer had an optimal response because its LDH release was minimum, associated with the best crystallinity of this single layer, which generates a higher roughness than multilayers. Additionally, the highest cytotoxicity, after Cu (reference) and 316L SS, was for the Al_2O_3 single layer, due to its amorphous nature and a relatively high corrosion rate. So, considering that the top layer is Al_2O_3, the multilayers would not present a viable solution for biocompatibility applications because of its high cytotoxicity. This work demonstrated that nanolaminates reduced from high to medium cytotoxicity grade. To improve the cytotoxic response and biocompatibility of $[Al_2O_3/ZnO]_n$/316L nanolaminates, we recommend changing the top-layer Al_2O_3 for ZnO ($[ZnO/Al_2O_3]_n$ multilayer system) in samples with $n = 1$ and $n = 2$.

This method is a very reliable one to produce continuous and fine layers with uniform properties on the surface they are applied to. Nevertheless, its cost is high and limited in the thickness that can be obtained, although this is compensated for by using a more economical substrate in biomedical applications.

Author Contributions: Conceptualization, H.T., J.C.C. and G.Z.; Data curation, D.O., J.L., M.A.H.-L., M.R.-C. and G.Z.; Formal analysis, D.O., M.A.H.-L. and M.R.-C.; Funding acquisition, H.T., M.H.F., J.M.Y.-L. and G.Z.; Investigation, D.O., J.L., M.H.F., J.M.Y.-L., J.O.G., J.C.C. and G.Z.; Methodology, G.Z.; Project administration, G.Z.; Resources, J.L. and J.O.G.; Supervision, G.Z.; Validation, J.L., M.A.H.-L., M.R.-C., J.O.G. and G.Z.; Visualization, G.Z.; Writing—original draft, D.O., J.L., H.T., M.H.F., M.A.H.-L., M.R.-C., J.M.Y.-L.

and G.Z.; Writing—review & editing, G.Z. All authors have read and agreed to the published version of the manuscript.

Conflicts of Interest: The authors declare no conflict of interest.

References

1. Tlili, B.; Nouveau, C.; Walock, M.; Nasri, M.; Ghrib, T. Effect of layer thickness on thermal properties of multilayer thin films produced by PVD. *Vacuum* **2012**, *86*, 1048–1056. [CrossRef]
2. Ott, A.W.; Klaus, J.W.; Johnson, J.M.; George, S.M.; Oro, L.A. Al3O3 thin film growth on Si (100) using binary reaction sequence chemistry. *Thin Solid Films* **1997**, *292*, 135–144. [CrossRef]
3. Elam, J.W.; George, S.M. Growth of ZnO/Al_2O_3 alloy films using atomic layer deposition techniques. *Chem. Mater.* **2003**, *15*, 1020–1028. [CrossRef]
4. Elam, J.W.; Sechrist, Z.A.; George, S.M. ZnO/Al_2O_3 nanolaminates fabricated by atomic layer deposition: Growth and surface roughness measurements. *Thin Solid Films* **2002**, *414*, 43–55. [CrossRef]
5. Tirado, S. Thin Films of Zinc Oxide Doped with Aluminium and Fluoride Prepared by Sol-Gel. *Av. Cienc. Igenieria* **2012**, *3*, 87–96.
6. López, J.; Martínez, J.; Abundiz, N.; Domínguez, D.; Murillo, E.; Castillón, F.F.; Machorro, R.; Farías, M.H.; Tiznado, H. Thickness effect on the optical and morphological properties in Al_2O_3/ZnO nanolaminate thin films prepared by atomic layer deposition. *Superlattices Microstruct.* **2016**, *90*, 265–273. [CrossRef]
7. Lopez, J.; Solorio, E.; Borbón-Nuñez, H.A.; Castillón, F.F.; Machorro, R.; Nedev, N.; Farías, M.H.; Tiznado, H. Refractive index and bandgap variation in Al_2O_3-ZnO ultrathin multilayers prepared by atomic layer deposition. *J. Alloys Compd.* **2017**, *691*, 308–315. [CrossRef]
8. Liu, H.; Yang, R.B.; Guo, S.; Lee, C.J.J.; Yakovlev, N.L. Effect of annealing on structural and optical properties of ZnO/Al_2O_3 superlattice structures grown by atomic layer deposition at 150 °C. *J. Alloys Compd.* **2017**, *703*, 225–231. [CrossRef]
9. Homola, T.; BuršÝkovß, V.; Ivanova, T.V.; Souček, P.; Maydannik, P.S.; Cameron, D.C.; Lackner, J.M. Mechanical properties of atomic layer deposited Al_2O_3/ZnO nanolaminates. *Surf. Coat. Technol.* **2015**, *284*, 198–205. [CrossRef]
10. Chaaya, A.A.; Viter, R.; Baleviciute, I.; Bechelany, M.; Ramanavicius, A.; Gertnere, Z.; Erts, D.; Smyntyna, V.; Miele, P. Tuning optical properties of Al_2O_3/ZnO nanolaminates synthesized by atomic layer deposition. *J. Phys. Chem. C* **2014**, *118*, 3811–3819. [CrossRef]
11. Wang, X.O.; Ding, J.N.; Yuan, N.Y.; Cheng, G.G.; Zhu, Y.Y.; Kan, B. Mechanical property of nanoscale ZnO/Al_2O_3 multilayers: An investigation by nano-indentation. In Proceedings of the 8th Annual IEEE International Conference on Nano/Micro Engineered and Molecular Systems, Suzhou, China, 7–10 April 2013; pp. 1222–1225. [CrossRef]
12. Guchhait, S.K.; Paul, S. Synthesis and characterization of $ZnO-Al_2O_3$ oxides as energetic electro-catalytic material for glucose fuel cell. *J. Fuel Chem. Technol.* **2015**, *43*, 1004–1010. [CrossRef]
13. Li, Z.; Yang, R.; Yu, M.; Bai, F.; Li, C.; Wang, Z.L. Cellular Level Biocompatibility and Biosafety of ZnO Nanowires. *J. Phys. Chem. C* **2008**, *112*, 20114–20117. [CrossRef]

14. Rogé, V.; Georgantzopoulou, A.; Mehennaoui, K.; Fechete, I.; Garin, F.; Dinia, A.; Gutleb, A.C.; Lenoble, D. Tailoring the optical properties of ZnO nano-layers and their effect on in vitro biocompatibility. *RSC Adv.* **2015**, *5*, 97635–97647. [CrossRef]

15. Oprea, O.; Andronescu, E.; Ficai, D.; Ficai, A.; Oktar, F.; Yetmez, M. ZnO Applications and Challenges. *Curr. Org. Chem.* **2014**, *18*, 192–203. [CrossRef]

16. Kołodziejczak-Radzimska, A.; Jesionowski, T. Zinc oxide—from synthesis to application: A review. *Materials* **2014**, *7*, 2833–2881. [CrossRef] [PubMed]

17. Zhang, W.C.Y.; Nayak, T.R.; Hong, H. Biomedical Applications of Zinc Oxide Nanomaterials. *Curr. Mol. Med.* **2013**, *13*, 1633–1645. [CrossRef]

18. Özgür, Ü.; Alivov, Y.I.; Liu, C.; Teke, A.; Reshchikov, M.A.; Dogan, S.; Avrutin, V.; Cho, S.-J.; Morkoç, H. A comprehensive review of ZnO materials and devices. *J. Appl. Phys.* **2005**, *98*, 1–103. [CrossRef]

19. Nevarez-Rascon, A.; González-Lopez, S.; Acosta-Torres, L.S.; Nevarez-Rascon, M.M.; Borunda, E.O. Synthesis, biocompatibility and mechanical properties of ZrO_2-Al_2O_3 ceramics composites. *Dent. Mater. J.* **2016**, *35*, 392–398. [CrossRef]

20. George, S.M. Atomic Layer Deposition: An Overview. *Chem. Rev.* **2010**, *110*, 111–131. [CrossRef]

21. Kukli, K.; Salmi, E.; Jõgiaas, T.; Zabels, R.; Schuisky, M.; Westlinder, J.; Mizohata, K.; Ritala, M.; Leskelä, M. Atomic layer deposition of aluminum oxide on modified steel substrates. *Surf. Coat. Technol.* **2016**, *304*, 1–8. [CrossRef]

22. Leskelä, M.; Ritala, M. Atomic layer deposition chemistry: Recent developments and future challenges. *Angew. Chem. Int. Ed.* **2003**, *42*, 5548–5554. [CrossRef] [PubMed]

23. Finch, D.S.; Oreskovic, T.; Ramadurai, K.; Herrmann, C.F.; George, S.M.; Mahajan, R.L. Biocompatibility of atomic layer-deposited alumina thin films. *J. Biomed. Mater. Res. Part A* **2008**, *87*, 100–106. [CrossRef]

24. Marin, E.; Guzman, L.; Lanzutti, A.; Ensinger, W.; Fedrizzi, L. Multilayer Al_2O_3/TiO_2 Atomic Layer Deposition coatings for the corrosion protection of stainless steel. *Thin Solid Films* **2012**, *522*, 283–288. [CrossRef]

25. Beche, E.; Fournel, F.; Larrey, V.; Rieutord, F.; Morales, C.; Charvet, A.-M.; Madeira, F.; Audoit, G.; Fabbri, J.-M. Direct Bonding Mechanism of ALD-Al_2O_3 Thin Films. *ECS J. Solid State Sci. Technol.* **2015**, *4*, P171–P175. [CrossRef]

26. Nguyen, H.M.T.; Tang, H.-Y.; Huang, W.-F.; Lin, M.C. Mechanisms for reactions of trimethylaluminum with molecular oxygen and water. *Comput. Theor. Chem.* **2014**, *1035*, 39–43. [CrossRef]

27. Martínez, E.G.; Flores, J.A.; Tijerina, E.P. Depósito de películas ultradelgadas de óxido de zinc (ZnO) por ALD. *CIENCIA-UANL* **2010**, *13*, 247–253.

28. Weckman, T.; Laasonen, K. Atomic layer deposition of zinc oxide: Diethyl zinc reactions and surface saturation from first-principles. *J. Phys. Chem. C* **2016**, *120*, 21460–21471. [CrossRef]

29. Guerrero-Sánchez, J.; Borbon-Nunez, H.A.; Tiznado, H.; Takeuchi, N. Understanding the first half-ALD cycle of the ZnO growth on hydroxyl functionalized carbon nanotubes. *Phys. Chem. Chem. Phys.* **2020**, *19*, accepted. [CrossRef]

30. Science, R.A. Cytotoxicity Detection Kit Plus (LDH). 2016, pp. 1–24. Available online: https://www.sigmaaldrich.com/content/dam/sigma-aldrich/docs/Roche/Bulletin/1/cytodetrobul.pdf (accessed on 6 July 2020).

31. Kaja, S.; Payne, A.J.; Naumchuk, Y.; Koulen, P. Quantification of lactate dehydrogenase for cell viability testing using cell lines and primary cultured astrocytes. *Curr. Protoc. Toxicol.* **2017**, *2017*, 1–10. [CrossRef]

32. Al-Gaashani, R.; Radiman, S.; Daud, A.R.; Tabet, N.; Al-Douri, Y. XPS and optical studies of different morphologies of ZnO nanostructures prepared by microwave methods. *Ceram. Int.* **2013**, *39*, 2283–2292. [CrossRef]

33. Scardi, P.; Ermrich, M.; Fitch, A.; Huang, E.W.; Jardin, R.; Kuzel, R.; Leineweber, A.; Mendoza Cuevas, A.; Misture, S.T.; Rebuffi, L.; et al. Size–strain separation in diffraction line profile analysis. *J. Appl. Crystallogr.* **2018**, *51*, 831–843. [CrossRef] [PubMed]

34. Jlassi, M.; Sta, I.; Hajji, M.; Ezzaouia, H. Effect of nickel doping on physical properties of zinc oxide thin films prepared by the spray pyrolysis method. *Appl. Surf. Sci.* **2014**, *301*, 216–224. [CrossRef]

35. Benramache, S.; Belahssen, O.; Arif, A.; Guettaf, A. A correlation for crystallite size of undoped ZnO thin film with the band gap energy—Precursor molarity—Substrate temperature. *Optik (Stuttg)* **2014**, *125*, 1303–1306. [CrossRef]

36. Xiao, S.S.; Zhao, L.; Liu, Y.H.; Lian, J.S. Nanocrystalline ZnO films prepared by pulsed laser deposition and their abnormal optical properties. *Appl. Surf. Sci.* **2013**, *283*, 781–787. [CrossRef]

37. Iatsunskyi, I.; Kempiński, M.; Jancelewicz, M.; Załęski, K.; Jurga, S.; Smyntyna, V. Structural and XPS characterization of ALD Al_2O_3 coated porous silicon. *Vacuum* **2015**, *113*, 52–58. [CrossRef]

38. Reddy, N.; Bera, P.; Reddy, V.R.; Sridhara, N.; Dey, A.; Anandan, C.; Sharma, A.K. XPS study of sputtered alumina thin films. *Ceram. Int.* **2014**, *40*, 11099–11107. [CrossRef]

39. Djebaili, K.; Mekhalif, Z.; Boumaza, A.; Djelloul, A. XPS, FTIR, EDX, and XRD analysis of Al2O3 scales grown on PM2000 alloy. *J. Spectrosc.* **2015**, *2015*, 1–16. [CrossRef]

40. Das, J.; Pradhan, S.K.; Sahu, D.; Mishra, D.K.; Sarangi, S.; Nayak, B.B.; Verma, S.; Roul, B. Micro-Raman and XPS studies of pure ZnO ceramics. *Phys. B Condens. Matter* **2010**, *405*, 2492–2497. [CrossRef]

41. Li, D.H.; Zhai, C.H.; Zhou, W.C.; Huang, Q.H.; Wang, L.; Zheng, H.; Chen, L.; Chen, X.; Zhang, R.J. Effects of Bilayer Thickness on the Morphological, Optical, and Electrical Properties of Al2O3/ZnO Nanolaminates. *Nanoscale Res. Lett.* **2017**, *12*. [CrossRef]

42. Martínez-Castelo, J.R.; López, J.; Domínguez, D.; Murillo, E.; Machorro, R.; Borbón-Nuñez, H.A.; Fernandez-Alvarez, I.; Arias, A.; Curiel, M.; Nedev, N.; et al. Structural and electrical characterization of multilayer Al2O3/ZnO nanolaminates grown by atomic layer deposition. *Mater. Sci. Semicond. Process.* **2017**, *71*, 290–295. [CrossRef]

43. Randles, J.E.B. Kinetics of rapid electrode reactions. *Discuss. Faraday Soc.* **2017**, *1*, 11–19. [CrossRef]

44. Surviliene, S.; Bellozor, S.; Kurtinaitiene, M.; Safonov, V. Protective properties of the chromium–titanium carbonitride composite coatings. *Surf. Coat. Technol.* **2004**, *176*, 193–201. [CrossRef]

45. Stern, M.; Geaby, A.L.; Geary, A. Electrochemical polarization I. A theoretical analysis of the shape of polarization curves. *J. Electrochem. Soc.* **1957**, *104*, 56–63. [CrossRef]

46. Inc, T.F.S. Intructions Pierce LDH Cytotoxicity Assay Kit. *Thermo. Sci* **2014**, *0747*, 1–7.

47. Provided, M.I. Biological evaluation of medical devices—Part 5: Tests for in vitro cytotoxicity Objectives and uses of AAMI standards and recommended practices. In *American National Standard*; Standard, A.N., Ed.; Association for the Advancement of Medical Instrumentation: Arlington, VA, USA, 2009; pp. 1–34. ISBN 1570203555.